Journal of Rock Mechanics and Geotechnical Engineering 14 (2022) 1064–1076

Contents lists available at ScienceDirect

Journal of Rock Mechanics and Geotechnical Engineering

journal homepage: www.jrmge.cn

Full Length Article

Development of a monitoring and warning system based on optical fiber sensing technology for masonry retaining walls and trees

Peichen Wu, Daoyuan Tan*, Shaoqun Lin, Wenbo Chen, Jianhua Yin, Numan Malik, An Li

Department of Civil and Environmental Engineering, The Hong Kong Polytechnic University, Hong Kong, China

ARTICLE INFO

Article history:
Received 18 May 2021
Received in revised form
15 August 2021
Accepted 9 September 2021
Available online 30 November 2021

Keywords:
Masonry retaining walls
Tree
Monitoring
Fiber Bragg grating (FBG) sensing
Warning system

ABSTRACT

Hong Kong has a long history of applying masonry retaining walls to provide horizontal platforms and stabilize man-made slopes. Due to the sub-tropical climate, some masonry retaining walls are colonized by trees. Extreme weather, such as typhoons and heavy rains, may cause rupture or root failure of those trees, thus resulting in instability of the retaining walls. A monitoring and warning system for the movement of masonry retaining walls and sway of trees has been designed with the application of fiber Bragg grating (FBG) sensing technology. The monitoring system is also equipped with a solar power system and 4G data transmission devices. The key functions of the proposed monitoring system include remote sensing and data access, early warning, and real-time data visualization. The setups and working principles of the monitoring systems and related transducers are introduced. The feasibility, accuracy, serviceability and reliability of this monitoring system have been checked by in-site calibration tests and four-month monitoring. Besides, a two-level interface has been developed for data visualization. The monitoring results show that the monitored masonry retaining wall had a reversible movement up to 2.5 mm during the monitoring period. Besides, it is found that the locations of the maximum strain on trees depend on the crown spread of trees.

1. Introduction

Old masonry retaining walls constructed according to traditional Chinese masonry techniques can be commonly found in urban Hong Kong for providing horizontal platforms and stabilized man-made slopes (Jim and Chen, 2010). Those old masonry retaining walls together with spontaneous vegetation on the surface create unique vertical habitats in Hong Kong. Trees growing on the masonry walls are identified as stonewall trees (Greening, Landscape and Tree Management Section, Development Bureau, 2013). Although most stonewall trees are strongly anchored with their colonized walls, failure may occur under intensive wind loads during extreme weathers, such as typhoons that threaten Hong Kong every year. In 2018, Hong Kong was stricken by a super-typhoon, *Mangkhut*, which was the most severe storm to ever hit the city since the records began in 1946 (Abbas et al., 2020). Accompanied strong winds and torrential rain have caused disastrous damages to both human and ecosystem.

Due to the high ecological and cultural values of stonewall trees and masonry retaining walls, those structures in service are in great need of intelligent health monitoring systems to evaluate their deformation and safety, and further control their possible failures. In this study, optical fiber sensing technology is innovatively applied to monitoring the movement of masonry retaining walls and the sway motion of stonewall trees and large trees.

Apart from the monitoring systems based on conventional electronic sensors, optical fiber sensing techniques, such as fiber Bragg grating (FBG), Brillouin optical-fiber time-domain analysis (BOTDA), Brillouin optical time-domain reflectometer (BOTDR), and optical frequency domain reflectometry (OFDR), have been successfully used for structure health monitoring (Pei et al., 2014; Hong et al., 2017; Xu et al., 2018; Feng et al., 2019). For the innovative application of fiber optical sensing technology in engineering geology, it has been successfully used for slope stability analyses, landslide prediction, and early warning of other geohazards (Zhu et al., 2014, 2017a, b; Chen et al., 2019; Zhang et al., 2019, 2020, 2021; Li et al., 2020; Shi et al., 2021; Xiong et al., 2021). Table 1 summarizes the pros and cons of common monitoring methods

* Corresponding author.
E-mail address: dao.y.tan@polyu.edu.hk (D. Tan).

Peer review under responsibility of Institute of Rock and Soil Mechanics, Chinese Academy of Sciences.

https://doi.org/10.1016/j.jrmge.2021.09.013

Table 1
Comparison of monitoring systems based on different sensing techniques.

Method	Pros	Cons	Application
Monitoring system based on FBG technology	Quasi-distributed sensing, real-time monitoring, suitable for both static and dynamic monitoring, suitable for the measurement under extreme weather, easy for multiplexing, high accuracy and stability	Costly, fragile if no protection, strain measurement within 1%	Monitoring of structures, geohazards, earth structures, and dynamic behavior trees (Pei et al., 2013; Hong et al., 2016; Zhu et al., 2017a,b; Li et al., 2020; Wu et al., 2021)
Monitoring system based on distributed fiber optic sensing (DFOS) technology	Fully distributed sensing, real-time monitoring, good for quasi-static or low-frequency application, suitable for the measurement under extreme weathers	Not efficient for long-distance dynamic monitoring (Cazzulani et al., 2021), strain measurement within 1%	Monitoring of pipes, slopes, landslides and earth structures (Ni et al., 2018; Zhang et al., 2018, 2020, 2021; Feng et al., 2019)
Monitoring system based on prisms	Real-time monitoring, suitable for both static and dynamic monitoring, high accuracy	Discrete sensing, complicated setup, small measurement range	Monitoring of sway motion of trees (Hassinen et al., 1998)
Monitoring system based on laser-related techniques	Real-time monitoring, suitable for both static and dynamic monitoring, high accuracy	Not suitable for typhoon conditions, discrete sensing	Structural health monitoring and natural frequency measurement of trees (Baker, 1997; Staszewski et al., 2004; Park et al., 2007)
Monitoring system based on conventional electronic sensors	Real-time monitoring, suitable for both static and dynamic monitoring, economical	Not suitable for thunderstorm or heavy rain conditions, discrete sensing, hysteresis and sensor drift	Monitoring of structures, earth structures (Admassu et al., 2019; Katsuda et al., 2019)

based on state-of-the-art sensing techniques. From the comparison, it can be seen that FBG technology can be a promising technique for dynamic monitoring of structures. The first FBG sensor was invented by Hill et al. (1978). Since then, FBG sensing technology has become the most widely used optical fiber sensing technology for strain and temperature measurement. FBG sensing technology shows its advantages in high accuracy, good reliability, immunity to electromagnetic interference, and capacity of multiplexing. Therefore, this technology has been utilized in this study for monitoring masonry retaining walls, stonewall trees, and large trees, which may be at risk or subjected to failure when exposed to severe weather such as typhoons, heavy rains, increase of groundwater or water pressure.

2. Monitoring and warning system

2.1. Overview of monitoring and warning system

The monitoring system developed for this study consists of (a) transducers based on FBG sensing technology, (b) data acquisition system, (c) data processing system, (d) remote data transmission module, and (e) solar power system, as shown in Fig. 1. Optical signals of transducers installed on masonry retaining walls and trees are detected by the data acquisition system and transferred to the data processing system for data analysis. Figures reflecting the dynamic movement of monitored masonry retaining walls and deflection of monitored trees can be plotted and presented on a visualized user interface by analyzing the real-time data of the transducers. Threshold values for both movement of masonry retaining walls and sway of trees can be pre-set. Warning or alarm messages will be distributed to the pre-assigned distribution list once those threshold values are exceeded.

2.2. Transducers and sensing principles

The bulging deformation of masonry retaining walls is monitored by measuring beams equipped with FBG sensors. The strain and tilt angle of trees are monitored by self-designed FBG-based strain gauges and tiltmeters, respectively.

2.2.1. FBG sensors and FBG sensing technology

An FBG is a periodic perturbation of the core refractive index along the optical fiber length which is formed by exposure of the core of the fiber to an intense optical interference pattern (Hill and Meltz, 1997). Optical fibers with FBG can directly transform the sensed parameter to the optical wavelength, which is independent of the optical energy, light level and fiber losses. The structure of an FBG sensor is illustrated in Fig. 2. Nowadays, a variety of measurement methods based on FBG sensing technology have been developed to substitute for conventional electro-mechanical sensor systems for different measurands and applications (Xu et al., 2013; Hong et al., 2016; Zhu et al., 2017a,b; Qin et al., 2020).

The rationale of operating an FBG sensor system is to detect the wavelength shift of reflected "Bragg" light as a function of the measurand. The reflected Bragg wavelength (λ_B) is determined by both the effective core refractive index of the fiber (n_{eff}) and the grating period (Λ), and the relationship is expressed as follows (Morey et al., 1990):

$$\lambda_B = 2n_{eff}\Lambda \tag{1}$$

The Bragg wavelength is sensitive to both strain and temperature. Strain causes both the change in the grating period owing to physical elongation of the fiber and the change in fiber refractive index due to photo-elastic effect, while temperature produces both the thermal expansion of the fiber and the change in fiber refractive index due to thermo-optic effect (Morey et al., 1990). For a single-mode silica fiber, the Bragg wavelength shift ($\Delta\lambda_B$) induced by the strain change ($\Delta\varepsilon$) and temperature variation (ΔT) is given by (Morey et al., 1990; Hill and Meltz, 1997):

$$\frac{\Delta\lambda_B}{\lambda_{B0}} = (1-p_e)\Delta\varepsilon + (\alpha+\xi)\Delta T = c_\varepsilon\Delta\varepsilon + c_T\Delta T \tag{2}$$

where λ_{B0} is the original Bragg wavelength; p_e is the effective photo-elastic coefficient; α is the thermal expansion coefficient of the fiber material; ξ is the thermo-optic coefficient; c_ε and c_T represent the coefficients of strain and temperature with the typical values of 0.78 and 6.67×10^{-6} °C^{-1}, respectively.

Rearranging Eq. (2), the strain detected by FBG sensors can be calculated by

$$\varepsilon = \Delta\varepsilon + \varepsilon_0 = \frac{1}{c_\varepsilon}\left(\frac{\Delta\lambda_B}{\lambda_{B0}} - c_T\Delta T\right) + \varepsilon_0 \tag{3}$$

where ε is the measured strain, and ε_0 is the initial strain. The temperature variation (ΔT) can be measured by placing an additional FBG sensor (temperature compensation sensor), free of any

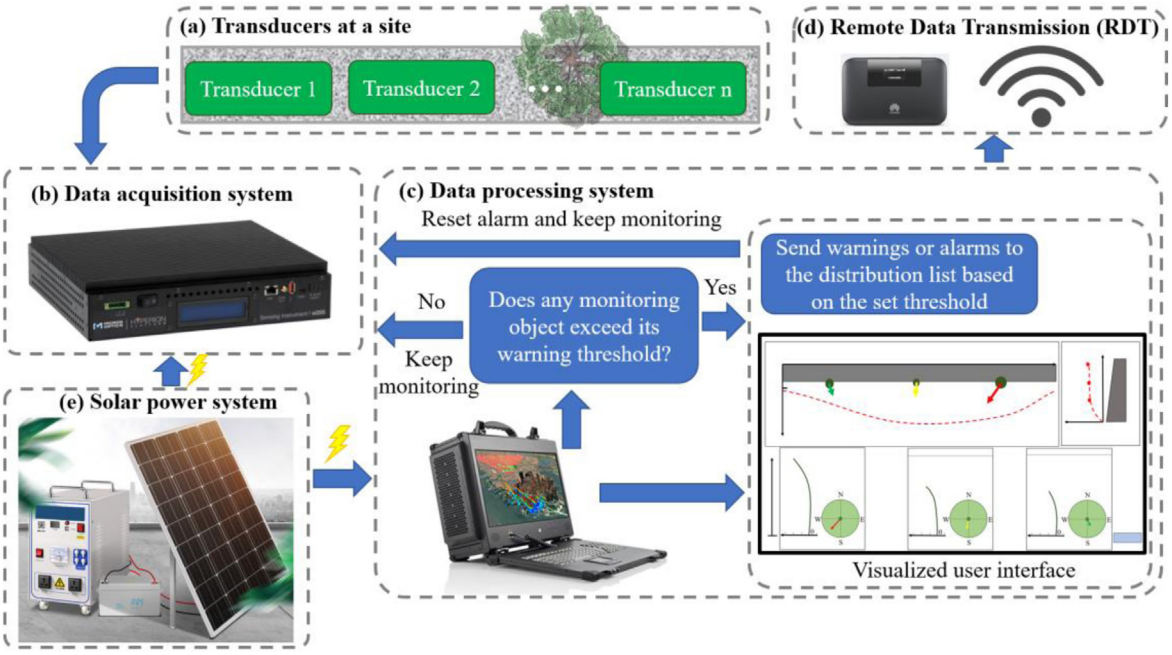

Fig. 1. Illustration of the monitoring system.

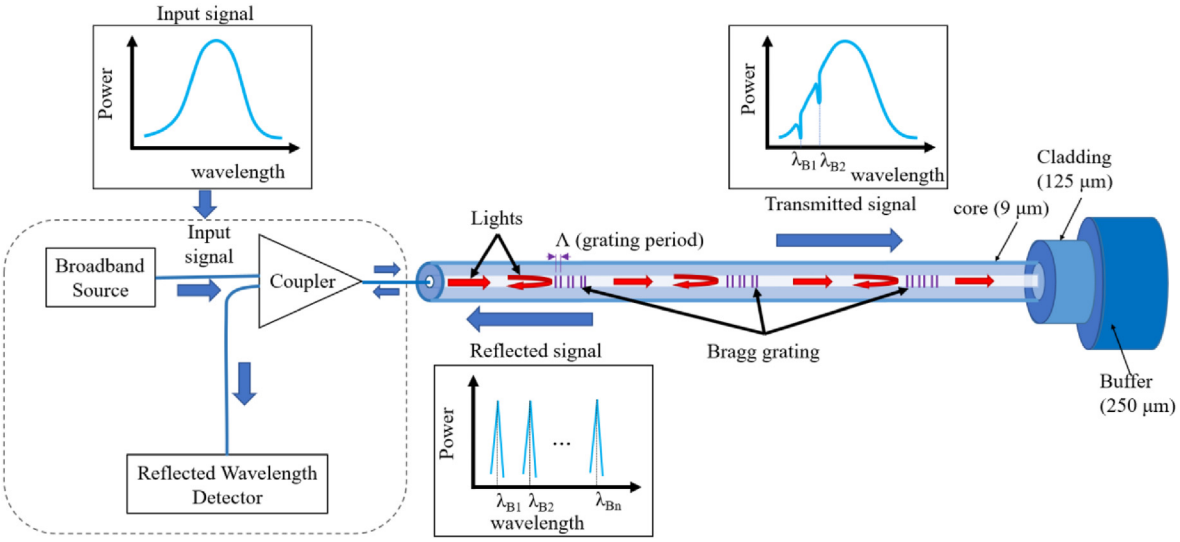

Fig. 2. Scientific principle of FBG sensing technology and the structure of an FBG sensor.

mechanical strain and only thermal-induced, to the same temperature field. The basic information of the FBG sensors used in this study is listed in Table 2.

Table 2
Basic information of the FBG sensors used in this study.

Item	Specification
Center wavelength	1510–1580 nm
FBG length	10 mm
Reflectivity	≥90%
Bandwidth at 3 dB	≤0.3 nm
Fiber type	SMF-28e
Coating	Acrylate

Note: Coating was removed at the locations of FBGs.

2.2.2. Bulging deformation of masonry retaining walls

Measurement of the bulging deformation of masonry retaining walls is based on the application of Euler–Bernoulli beam theory. Measuring beams are attached to the masonry wall by supporters. It is assumed that the supporters have high stiffness and the polyvinyl chloride (PVC) beam between two supporters can be regarded as a separated fixed beam. Those supporters are also regarded as measuring points of retaining walls. FBG sensors are attached to the measuring beams to detect the bending strain due to the relative displacement of the adjacent measuring points, as shown in Fig. 3. The relative displacement between two adjacent measuring points (Δ) can be therefore calculated using the following equation:

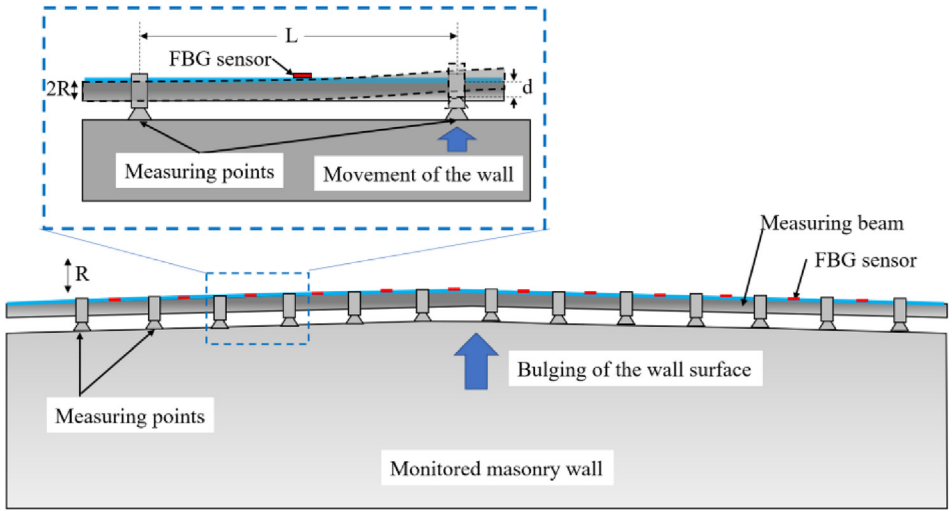

Fig. 3. Measurement of the movement of masonry walls.

$$\Delta = \frac{2\varepsilon L^2}{3R} \tag{4}$$

where R is the radius of the beam element, and L is the spacing of two measuring points. Based on the results of sensitivity analysis, a high displacement accuracy of ±0.1 mm can be reached by arranging the measuring points with a consistent spacing of 1 m and utilizing measuring beams with a diameter of 0.03 m.

It should be noted that the abovementioned setup is not able to distinguish the deformation along the wall and the deformation in the outward direction. For the measurement of the complex deformation combination, it is suggested to attach FBG sensors to both sides of the measuring beam. The deformation along the wall (e.g. tension cracks) can be detected by the axial strains after perfect temperature compensation, and the bulging deformation can be detected by the bending strains. Nevertheless, the movement along the wall is neglected compared with the bulging deformation of the wall since the monitored retaining wall is considered fix-ended at two horizontal ends.

2.2.3. Deflection and tilt of trees

For monitoring of the stonewall trees and large trees, the real-time deflections and tilt angles of the trees can be measured by the application of two types of self-developed innovative FBG-based transducers, i.e. FBG-based strain gauges and tiltmeters.

The FBG-based strain gauge is comprised of an FBG sensor and a polyoxymethylene (POM) backing, as shown in Fig. 4a. Self-tapping screws can be used for mounting the strain gauges on trees. The total length of the FBG-based strain gauges is 65 mm. The measured strain is the average value of the strains along the length covered by the strain gauge. The performance of the FBG-based strain gauges and the reliability of the strain measurement have been verified by laboratory and in situ tests. Detailed information can refer to Wu et al. (2021).

A pair of strain gauges should be installed perpendicular to each other at the same height of a tree, as shown in Fig. 4c. The strain at the given height on the tree can be expressed as a combination of two orthogonal components which are measured by the two strain gauges:

$$\varepsilon = \sqrt{\varepsilon_x^2 + \varepsilon_y^2} \tag{5}$$

where ε_x and ε_y can be calculated by Eq. (3).

A series of FBG sensors can be installed in a row along the tree trunk. More accurate strain distribution and deflection curve of the tree trunk can be obtained by densifying the transducer number. For a tree monitored by n FBG sensors, the corresponding deflection of the tree can be measured by solving an $n \times n$ matrix equation according to cantilever analogy (Pei et al., 2013):

$$\begin{bmatrix} d_2 \\ \vdots \\ d_{n+1} \end{bmatrix} = \frac{L^2}{D} \begin{bmatrix} 1 & 0 & \cdots & \cdots & 0 \\ -2 & \ddots & \ddots & \ddots & \vdots \\ 1 & \ddots & \ddots & \ddots & \vdots \\ \vdots & \ddots & \ddots & \ddots & 0 \\ 0 & \vdots & 1 & -2 & 1 \end{bmatrix}^{-1} \begin{bmatrix} \varepsilon_1 \\ \vdots \\ \varepsilon_n \end{bmatrix} \tag{6}$$

where d_{n+1} is the deflection value at the position of the n-th FBG sensor on the tree; D is the diameter of the monitored tree (constant diameter and perfect circular cross-section of the tree are assumed); and ε_n is the strain measured by the n-th FBG sensor, as illustrated in Fig. 4c. Considering that the dynamic responses of trees under wind loads are the main concern, it is assumed that the first section which is close to the root of the tree is fixed, giving that $d_1 = 0$. The calculated deflections of trees are used for data visualization, as shown in Fig. 5.

The FBG-based tiltmeter is comprised of a three-dimensional printed sensing bar with two FBG sensors attached perpendicular to each other, a weight made of lead with an FBG sensor for temperature compensation, and a metal shell for protection, as shown in Fig. 4b. The measured tilt angles can be obtained by the following equation:

$$\theta = \sqrt{a\left(\frac{\Delta\lambda_1}{\lambda_{1B}} - k_T\frac{\Delta\lambda_T}{\lambda_{TB}}\right)^2 + b\left(\frac{\Delta\lambda_2}{\lambda_{2B}} - k_T\frac{\Delta\lambda_T}{\lambda_{TB}}\right)^2} \tag{7}$$

where a and b are the calibrated parameters of a tiltmeter by laboratory calibration tests, λ_1 and λ_2 are the wavelengths of two FBG sensors for measuring angles, λ_T is the wavelength of the FBG sensor used for temperature compensation, the subscript B means initial value, and k_T is a coefficient of temperature compensation according to the temperature calibration test conducted in the laboratory. Thermal conductivities of the backing and outer materials of FBG-based tiltmeters have been considered and included in the determination of k_T during the calibration experiments. Based on the laboratory calibration experiments under a controlled environment, the resolutions of FBG-based strain gauge and tiltmeter can reach 10^{-6} and 0.1°, respectively.

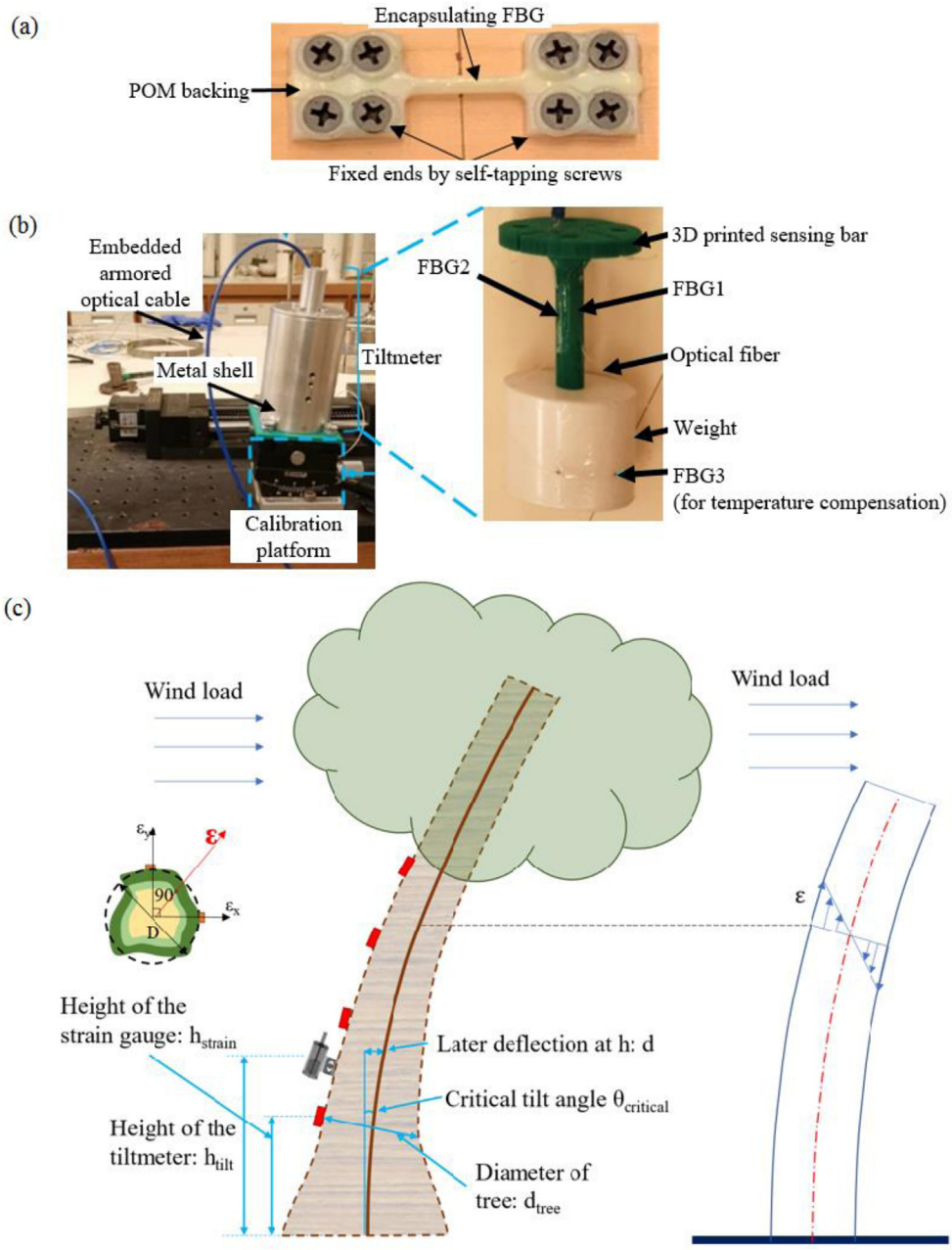

Fig. 4. (a) FBG-based strain gauge, (b) FBG-based tiltmeter, and (c) illustration of a monitored tree equipped with FBG-based strain gauges and tiltmeters.

2.3. Data processing system, remote accessibility and data visualization

Signals of the FBG sensors are detected by an optical sensing interrogator (si225, Luna Innovations, US). The interrogator is capable of measuring more than 300 FBG sensors at the maximum dynamic sampling rate of 1000 Hz simultaneously. Based on the experience of four-month monitoring, the recommended sampling rates based on the weather condition are given and listed in Table 3.

With the support of 4G data transmission technology, the data processing system at the monitoring site can be accessed remotely through desktop and mobile platforms. A two-level interface has been proposed for visualizing the monitored data. The first interface level reveals the real-time data of each transducer, which can be easily created in ENLIGHT software associated with the interrogator, as shown in Fig. 5a. Data visualization interface at this level has advantages in highlighting dangerous values and reporting warning signals. The second interface level is a self-developed application based on a self-developed MATLAB GUI program, which focuses on presenting the real-time deformation of the masonry retaining walls and real-time deflection and tilt angles of trees, as shown in Fig. 5b. This application shows its merits in providing timely intuitive figures for easily locating the critical locations and can be executed as a stand-alone application in any computer without the requirement of the MATLAB environment. Both the commercial software ENLIGHT and the self-developed application read the data from the interrogator directly, which can obtain the real-time dynamic behavior of the monitored walls and trees and not relies on the data saving interval.

Fig. 5. A two-level interface of data visualization based on (a) ENLIGHT software and (b) self-developed application.

2.4. Solar power system

The solar power system converts solar energy from sunlight into electricity, which allows the monitoring and warning system to work effectively in remote areas without external power supplies. The solar power system consists of a solar panel array, a rechargeable battery array, a DC (48 V)-AC (220 V) inverter, and a solar power controller, as shown in Fig. 6. The solar panel array is for electricity generation, whose power efficiency is designed based on the sunlight intensity and the total power requirement of the monitoring system. The battery array is to store the electrical energy generated by the solar panels during sunny days and provides electricity supply to the monitoring system during nights and rainy days. The DC-AC inverter is to provide a stable electricity supply to the monitoring system. The solar power controller is to maximize the energy harvest of the solar panel array and achieve full charge in the shortest possible time.

Table 3
Sampling rate under different weather conditions.

Weather condition	Data sampling rate (Hz)	Consideration
Issue of warning signals of tropical cyclone by the Hong Kong Observatory	100	Capture the dynamic behavior of monitored objectives and distribute timely warning and alarm messages (for dynamic monitoring)
Issue of warning signals of strong monsoon or rainstorm by the Hong Kong Observatory	10	Capture the dynamic behavior of monitored objectives (for dynamic monitoring)
Normal weather conditions	1	Monitor the working status of the monitoring system and avoid data redundancy (for static monitoring)

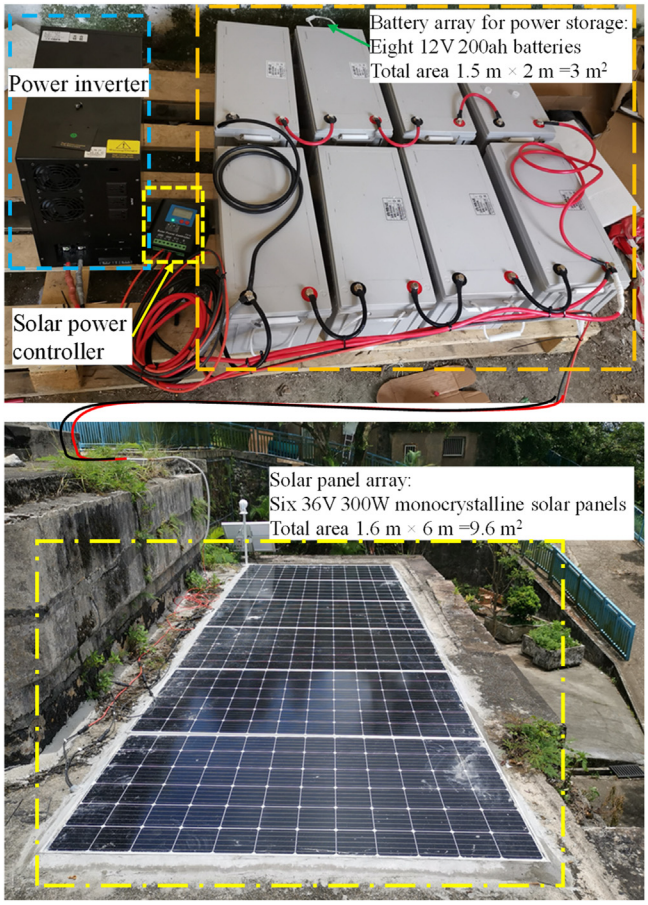

Fig. 6. The solar power system used in the monitoring site.

For the monitoring site that will be introduced in Section 3, six 1.6 m × 1 m solar panels were installed on the roof of a derelict building with a power efficiency of 36 V and 300 W. Redundancy of the power efficiency of the solar power array was designed to guarantee that this system can provide electricity supply to the monitoring system with the total power consumption of 200 W and charge the battery array during sunny days. Eight rechargeable batteries (200 Ah, 12 V) were used to guarantee that the monitoring system can continuously work for at least 5 d even the photovoltaic system cannot work efficiently during nights, cloudy and rainy days where the solar energy supply is insufficient.

3. Application of the monitoring and warning system

3.1. Site information

One of the monitoring sites of this study is located on a hilltop in Hong Kong Island, as shown in Fig. 7. One masonry retaining wall was selected to be monitored. This masonry retaining wall can be divided into two sections: a plain wall facing east and a curve wall facing south with a stonewall tree (*Ficus macrocarpa*, Chinese banyan) growing on it. To accurately measure the deformation and movement of the wall, the two sections are monitored individually by installing two sets of transducers, as shown in Fig. 8a. To be specific, two vertical and two longitudinal FBG-based measuring beams have been installed on the east surface of the masonry retaining wall to measure the bulging deformations of the wall surface. Two vertical and one longitudinal measuring beams were installed surrounding the stonewall tree to monitor possible wall deformation caused by the deflection of the stonewall tree. The stonewall trees (WT1) together with three large trees (T1, T2 and T3) adjacent to the masonry retaining wall were monitored. The basic information of those trees is listed in Table 4. For each tree, eight FBG-based strain gauges and two FBG-based tiltmeters were installed, as shown in Fig. 8b. The cost build-up for the entire monitoring system is listed in Table 5.

3.2. In-site calibration

In-site calibration tests have been conducted to verify the feasibility and accuracy of the deformation measurement of masonry retaining walls and strain measurement of trees using FBG sensors. The progress of the in-site calibration test is illustrated in Fig. 9. A displacement application system (a push device and a digimatic indicator) is utilized to precisely apply staged horizontal deformation to a measuring point between two adjacent FBG sensors (FBG_J1 and FBG_J2) on the PVC measuring beam for imitating the bulging deformation of the masonry retaining wall. Applied displacements at the measuring point induce strain changes which can be measured by adjacent FBG sensors. By comparing the measured strain with the applied displacement, a coefficient representing the relationship between the strain and the displacement can be obtained, as illustrated in Fig. 10. On the other hand, the theoretical coefficient can be calculated by Eq. (4). The difference between the theoretical and calibration results is mainly attributed to the relatively low stiffness of the beam supporters deviated from the assumption of fixed beam and the complicated condition of the masonry retaining wall, including the uncontrollable construction quality of the supporters for the measuring points and the rough surface of the masonry blocks. In addition, the beam theory considering pinned ends is also adopted to calculate the strain responses. The calibration results lie in between the theoretical results using different methods, as shown in Fig. 10. In that case, the coefficient obtained from the in-site calibration test is used for the measurement of bulging deformation in this study. Fig. 11 presents the results of the in-site calibration test conducted on T2 equipped with FBG-based strain gauges. The reference strain was measured by OFDR technology. The detailed calibration procedures and verification by OFDR technology can be found in Wu et al. (2021).

3.3. Determination of the threshold values

Intense wind loads, such as typhoons, usually cannot impose harmful loadings on masonry retaining walls but can cause rupture or root failure of trees. However, retaining walls colonized by stonewall trees have a higher chance of damage due to the failure of stonewall trees and induce safety hazards. Therefore, the primary consideration of the early warning system in this study lays on the stonewall tree (WT1) and large trees (T1, T2 and T3). It is necessary to set thresholds for measurands so that an early warning message including the warning information, maximum value and warning level can be sent to the pre-set distribution list once the thresholds are reached.

The monitored strain value can be a direct indicator to predict the occurrence of the possible trunk failure of trees. The trunk failure (rupture failure) mode starts when the stem exceeds its bending strength, which is usually defined as modulus of rupture (*MOR*). By introducing the modulus of elasticity (*MOE*) of trees, Hook's law can be used to perform tree risk assessment by measuring the strain of the risky tree trunk:

$$\varepsilon_{\text{critical}} = \frac{MOR}{MOE} FoS \tag{8}$$

where $\varepsilon_{\text{critical}}$ is the critical strain when the stem reaches its bending strength and faces a rupture failure, and *FoS* stands for the factor of safety. Considering the influence of the difference of tree species on *MOR*, an *FoS* of 70% is suggested for setting thresholds in this study (Peltola et al., 1999; Kane and Clouston, 2008). Referring to the statistical data provided by Liu et al. (2007) and Kane and Clouston (2008), the typical *MOR* is selected as 60 MPa, and the typical *MOE* is selected as 12 GPa. Therefore, a strain of 0.0035 is determined as the alarm threshold for indicating a rupture failure of a tree as a reference. The warning threshold is set as 0.8 times the alarm threshold, which is 0.0028. However, for common tree species in Hong Kong, further investigation is required to determine suitable and reliable *MOR*, *MOE* and *FoS*.

The monitored tilt angle can be a feasible indicator to predict the occurrence of the possible root failure of trees. The threshold of the tilt angle is determined from the profile of the tree trunk at the critical bending state when the critical strain occurs, as illustrated in Fig. 4c. By analyzing the relationship between the strain on the tree surface and the lateral deflection at the height of the tiltmeter, the following equation can be used to calculate the critical tilt angle of the tiltmeter:

$$\theta_{\text{critical}} = \arcsin \frac{d}{h_{\text{tilt}}} \tag{9}$$

where h_{tilt} is the installation height of the tiltmeter, d is the lateral deflection at the height of the tiltmeter and can be calculated by

$$d = \frac{2\varepsilon_{\text{critical}} h_{\text{tilt}}^3}{3(h_{\text{tilt}} - h_{\text{strain}})D} \tag{10}$$

where $\varepsilon_{\text{critical}}$ is the critical strain where the stem reaches its bending strength and faces a rupture failure. The critical tilt angles for all trees are determined based on the details of the instrument installation and the basic parameters of the trees, as listed in Table 6. It should be noted that the thresholds determined in this

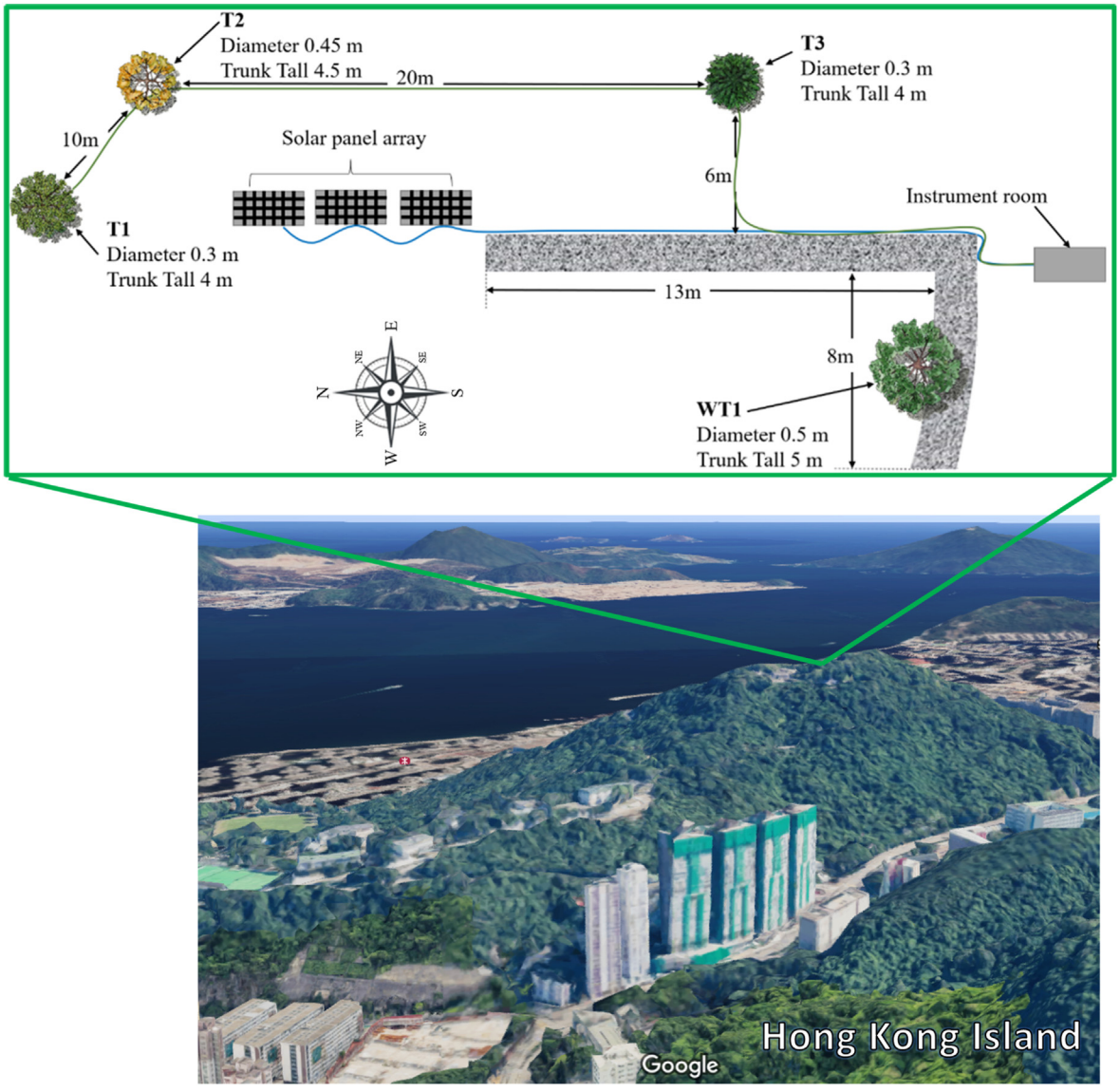

Fig. 7. Schematic diagram of the masonry retaining wall and trees at the monitoring site.

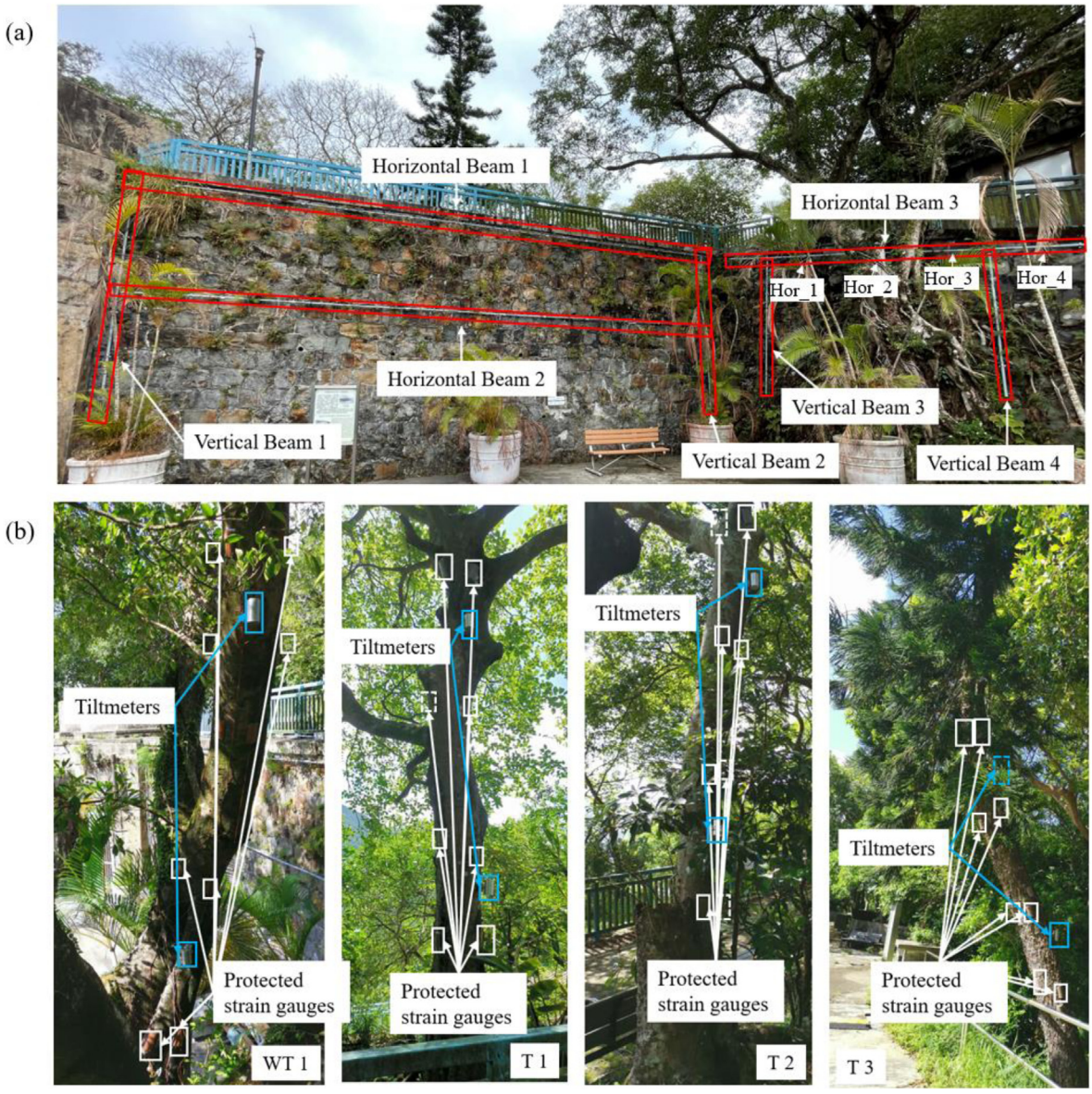

Fig. 8. (a) The layout of measuring beams on the monitored masonry retaining wall (Hor_1 to Hor_4 represent the data of different horizontal beam elements above the stonewall tree WT1)and (b) the layout of FBG-based strain gauges and tiltmeter on monitored trees.

Table 4
Basic information of monitored trees.

No. of tree	Type of tree	Scientific name of species	Installed height of strain gauges (m)	Installed height of tiltmeters (m)	Crown spread (m)	DBH (m)	Tree height (m)	Tree form
WT1	Stonewall tree	*Ficus microcarpa*	1.4, 2.2, 3.15, 4.15	1.8, 3.7	12	0.4	10	Spreading
T1	Large tree	*Celtis sinensis*	0.9, 1.8, 2.9, 3.8	1.6, 3.4	9	0.7	11	Spreading
T2	Large tree	*Celtis sinensis*	0.9, 1.9, 3, 4.05	1.5, 3.6	11	0.4	12	Spreading
T3	Large tree	*Araucaria cunninghamii*	1.3, 1.95, 2.95, 3.9	1.7, 3.6	3	0.6	8	Layered

Note: DBH represents the diameter at breast height.

study are only preliminary settings, which should be further reviewed and adjusted based on the dynamic behavior of the monitored trees to increase the accuracy of root failure prediction.

For the masonry retaining walls, the bulging deformation is mainly due to shear of joints between masonry blocks. According to Powrie et al. (2002), the maximum stable deflection is around 0.4–2.6 cm, depending on the stiffness of joints among masonry blocks. By measuring the typical sizes of the masonry blocks and conducting visual inspections, it was found that two joints can be covered within two adjacent measuring points on the masonry

Table 5
Cost build-up of the monitoring system.

Item	Unit	Unit price (HKD)	Quantity	Cost (HKD)
Instrumentation for monitoring a masonry retaining wall[a]	Set	26,000	1	26,000
Instrumentation for monitoring a tree[b]	Set	3800	4	15,200
Data processing system	Set	8000	1	8000
Remote data transmission assembly	Each	3000	1	3000
Optical sensing interrogator Model: si 255 (16 channels)	Each	400,000	1	400,000
4G/5G data transmission charge	Month	500	6	3000
Mini-computing centre	Each	10,000	1	10,000
Solar power supply system	Each	40,000	1	40,000
Total cost of the monitoring system at each site (HKD)[c]				505,200

[a] The total cost of the instrumentation for monitoring a tree is approximate 3800 HKD, which includes 8 FBG-based strain gauges (unit price: 100 HKD) and 2 tiltmeters (unit price: 500 HKD), and armored fiber optic cables (100 HKD/m, total length around 20 m).
[b] The total cost of instrumentation for monitoring the masonry retaining wall is approximate 26,000 HKD, which includes 50 FBG sensors (unit price: 100 HKD), 3 FBG-based LVDTs (unit price: 1000 HKD), measuring beams with protections (8000 HKD), and armored fiber optic cables (100 HKD/m, total length around 100 m).
[c] The cost of manpower is not included.

retaining wall. Therefore, the critical relative displacement between two measuring points is determined as $2 \times 2.6 = 5.2$ cm, yielding an alarming strain of approximately 0.0006 using the calibration results shown in Fig. 10. Similarly, the warning threshold is set as 0.8 time the alarm threshold, which is 0.00048.

4. Results and discussion

A four-month monitoring was conducted from September 2020 to December 2020, in which two typhoons (*Nangka* and *Saudel* in October) and several seasonal monsoons affected Hong Kong. Before the monitoring, resetting the initial readings for those sensors installed on the monitored trees before severe weathers is meaningful and necessary to obtain real responses under wind loads. In addition to the installation of individual temperature sensors, the temperature effect on the wavelength shift of the sensors installed on the monitored walls and trees can be eliminated automatically by implementing a low-pass filter. This process together with the abovementioned resetting can also eliminate the accumulated strain of those sensors installed on trees due to the gradual growth of the trees.

4.1. Deformation of masonry retaining walls

The deformation of the masonry retaining wall during the four-month monitoring period is plotted in Fig. 12. It can be found that the short-term bulging deformation with a magnitude of 2.5 mm can be detected by the measuring beam array. From a long-term point of view, the short-term deformation is reversible. Recovery of the deformation has been observed at the end of October and December. During our weekly site visits, no observable cracks were found on the masonry retaining wall. The temperature compensation was conducted by attaching parallel FBG sensors to the front and back sides of each section of the measuring beams. As we

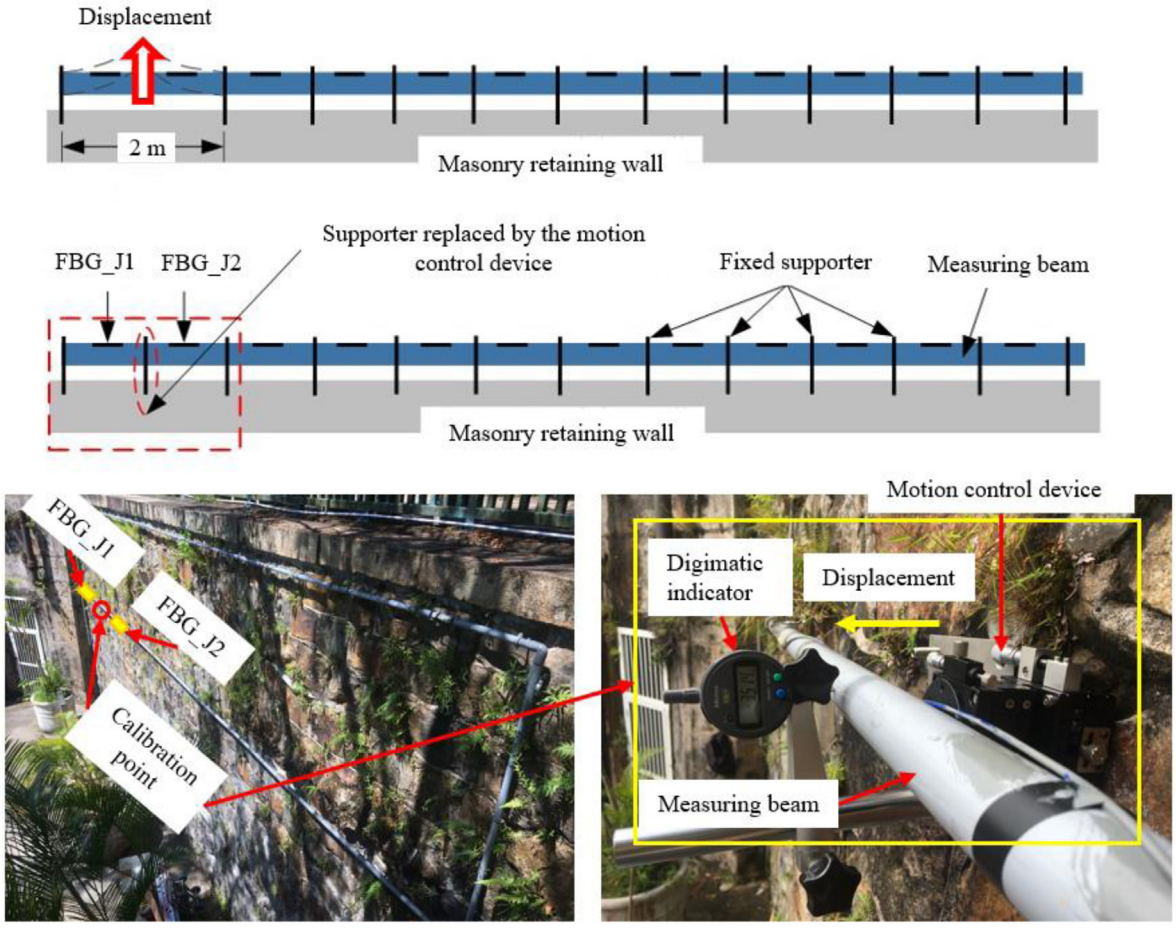

Fig. 9. Illustration of the in-site calibration on the masonry retaining wall.

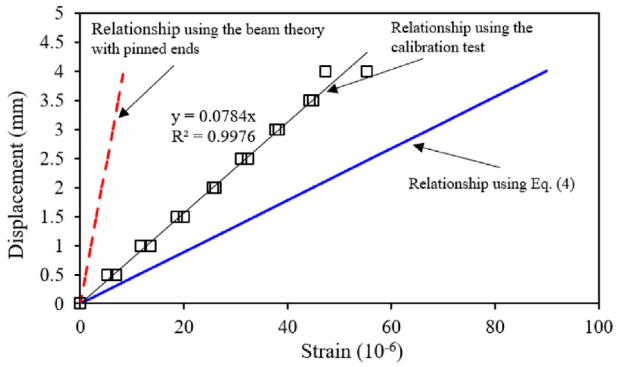

Fig. 10. Calibration results of deformation measurement of masonry retaining walls.

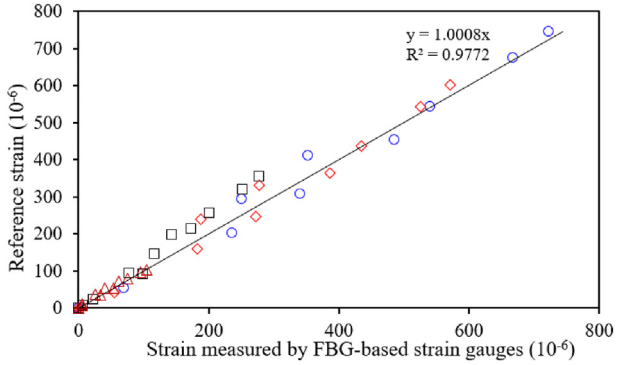

Fig. 11. Calibration results of FBG-based strain gauges on T2.

Table 6
Threshold of the critical strain and tilt angle.

Parameter	WT1	T1	T2	T3	Mansory retaining wall
$\varepsilon_{critical,warning}$ (10^{-6})	2800	2800	2800	2800	480
$\varepsilon_{critical,alarm}$ (10^{-6})	3500	3500	3500	3500	600
$\theta_{critical,warning}$ (°)	3.6	7.9	5.3	7.9	N/A
$\theta_{critical,alarm}$ (°)	4.5	9.9	6.7	9.9	N/A

expected, the stable monitoring results are independent of the gradual temperature decrease (see Fig. 12b) during the four-month monitoring period, which verifies the feasibility of this temperature compensation method. Fig. 12c presents the rainfall data during the monitoring period, showing that no obvious direct relationship between rainfall and wall movement can be observed in the magnitude of sub-millimeter.

4.2. Strains and tilt angles of monitored trees

Table 7 presents the maximum strains and tilt angles of the monitored trees in the four-month monitoring period. For each tree, the height of the location where the maximum strain occurred is marked. According to monitored data and the pre-set threshold, the monitored trees were in a safe condition throughout the monitoring period. It is interesting that T3 with the smallest crown spread (3 m) among the four monitored trees had the largest responses in terms of strain.

Fig. 13 shows the locations of the maximum strain of trees. It should be noted that the height of the location has been normalized by the height of the tree. Based on the monitoring results from September to December, it can be discovered that the locations of the

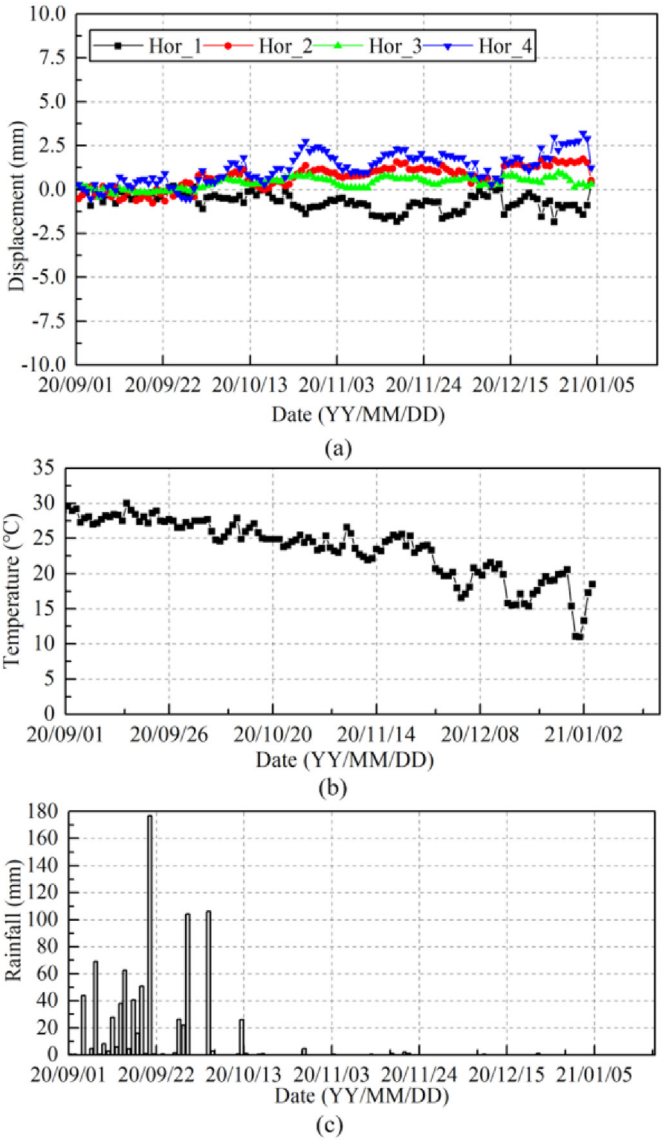

Fig. 12. (a) Displacement of the tree-colonized masonry retaining wall, (b) Temperature change, and (c) Rainfall during the four-month monitoring period.

Table 7
Maximum strains and tilt angles of monitored tress from September to December 2020.

Month	No. of tree	Maximum strain (10^{-6})/ height (m)	Maximum tilt angle (°)/height (m)
September	WT1	89/2.2	3.9/3.7
	T1	255/2.9	8.8/3.4
	T2	210/3	7.7/3.6
	T3	340/2.95	7.4/3.6
October	WT1	173/4.15	3.5/3.7
	T1	146/1.8	2.8/3.4
	T2	100/4.05	2.5/3.6
	T3	299/3.9	3.95/3.6
November	WT1	200/3.15	3/3.7
	T1	160/1.8	1.6/3.4
	T2	110/4.05	2.9/3.6
	T3	255/1.3	3.8/3.6
December	WT1	141.2/2.2	2.23/3.7
	T1	129.2/1.8	2.14/3.4
	T2	110/4.05	2.9/3.6
	T3	159.1/3.9	1.96/3.6

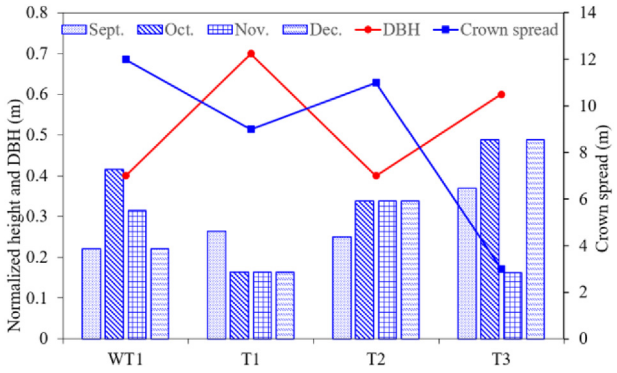

Fig. 13. Locations of the maximum strains on monitored trees with different values of DBH and crown spread.

maximum strains of all monitored trees are between 0.15 and 0.48 during October when two typhoons invaded Hong Kong including a Signal 8 typhoon (*Nangka*), which fits well with the finding by Kane and Clouston (2008) that the mean height of the rupture failure occurred at 26% of tree height. The crown spread and DBH of different trees are also plotted in Fig. 13. It can be seen that the locations of the maximum strain on different trees are irrelevant to DBH but somehow depend on the crown spread. For those trees with the crown spread larger than 8 m, the locations of the maximum strain occur at the lower part of the tree. For T3 with the crown spread of only 3 m, the location of the maximum strain varies significantly with time and tends to occur at the middle part of the tree.

A rose histogram is plotted to display the frequency of the sway motion of WT1 in different directions when typhoon *Nangka* hit Hong Kong, as shown in Fig. 14. The angular coordinator denotes the sway direction (angle) of the monitored trees. The radial coordinator denotes the frequency number of a sway angle. The larger the frequency number indicated by the radial coordinator at a specific angle, the higher the chance that the tree sways along the direction indicated by this angle. The dominant sway direction of the tree trunk at 4.15 m height is around 45°. At 3.15 m height, the dominant sway direction is around 0°. At 2.2 m height, the dominant sway direction is widely distributed from 90° to 150°. At 1.4 m height, the dominant sway direction is around 30°. Fig. 14b shows the sway directions in terms of the measured tilt angle in the upper part of WT1. The dominant sway direction was around 50°, which generally agrees with strain data. Based on the measured data from FBG-based strain gauges, natural frequencies of WT1, T1, T2 and T3 can be determined as 0.38 Hz, 0.58 Hz, 0.6 Hz and 0.45 Hz by conducting fast Fourier transformation (FFT) analysis.

As we can see from the monitored data of WT1, the typhoons and seasonal monsoons that occurred in the monitoring period give little effect on the reaction of this stonewall tree. Knowing that WT1 has a complicated canopy spreading around 12 m, the dynamic responses of the tree caused by intense wind loads can be largely attenuated due to the damping effect contributed by the canopy (James et al., 2006). Therefore, the force transmitted to the roots spread on the masonry retaining wall is reduced, which explains the negligible movement of the wall presented in Fig. 12.

5. Conclusions

A monitoring and warning system for the movement of masonry retaining walls and sway of adjacent trees under intense wind loads has been designed with the application of optical FBG sensing technology. The feasibility, accuracy, serviceability and reliability of this monitoring system have been checked by in-site calibration tests and four-month monitoring. The monitoring results show that

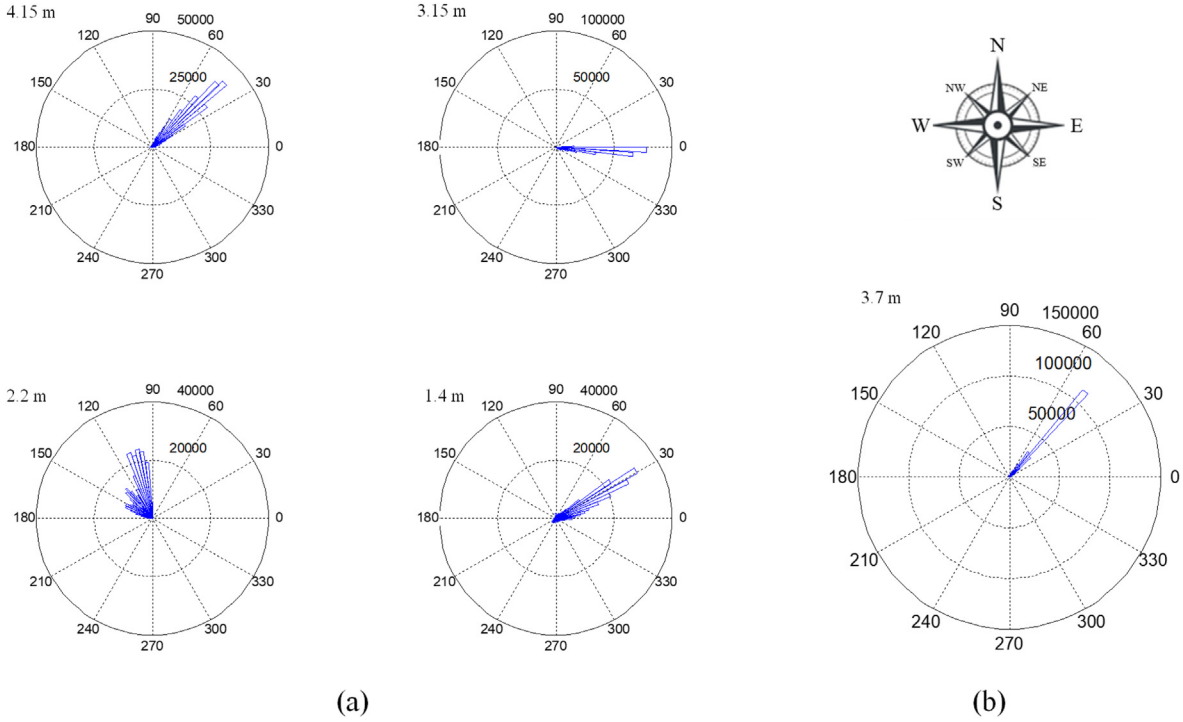

Fig. 14. Rose histograms of the sway directions in terms of (a) the strain and (b) the tilt angle of WT1 under typhoon *Nangka* in October 2020 (the angular coordinator denotes the sway direction in the unit of degree).

the masonry retaining wall had a reversible movement up to 2.5 mm during the monitoring period. Among the monitored trees, the one with a smaller crown spread tends to have a more significant response in strain. Besides, the locations of the maximum strain on different trees are irrelevant to the diameter of the tree trunk but depend on the crown spread due to the damping effect.

Declaration of competing interest

The authors declare that they have no known competing financial interests or personal relationships that could have appeared to influence the work reported in this paper.

Acknowledgments

The work in this paper is supported by the Development Bureau of Hong Kong SAR Government, a Research Impact Fund (RIF) project (Grant No. R5037-18), a Theme-based Research Scheme Fund (TRS) project (Grant No. T22-502/18-R), and a General Research Fund (GRF) projects (Grant No. PolyU 152130/19E) from Research Grants Council (RGC) of Hong Kong SAR. The authors also acknowledge the financial supports from Research Institute for Sustainable Urban Development of The Hong Kong Polytechnic University.

References

Abbas, S., Nichol, J.E., Fischer, G.A., Wong, M.S., Irteza, S.M., 2020. Impact assessment of a super-typhoon on Hong Kong's secondary vegetation and recommendations for restoration of resilience in the forest succession. Agric. For. Meteorol. 280, 107784.

Admassu, K.A., Lynch, J.P., Athanasopoulos-Zekkos, A., Zekkos, D., 2019. Long-term wireless monitoring solution for the risk management of highway retaining walls. In: Nondestructive Characterization and Monitoring of Advanced Materials, Aerospace, Civil Infrastructure, and Transportation XIII, vol. 10971, p. 1097103.

Baker, C.J., 1997. Measurements of the natural frequencies of trees. J. Exp. Bot. 48 (5), 1125–1132.

Cazzulani, G., Silva, A., Pennacchi, P., 2021. Optimization of continuous sensor placement for modal analysis: application to an optical backscatter reflectometry strain sensor. Mech. Syst. Signal Process. 150, 107242.

Chen, R.P., Zhang, P., Kang, X., Zhong, Z.Q., Liu, Y., Wu, H.N., 2019. Prediction of maximum surface settlement caused by EPB shield tunneling with ANN methods. Soils Found 59, 284–295.

Feng, W.Q., Yin, J.H., Borana, L., Qin, J.Q., Wu, P.C., Yang, J.L., 2019. A network theory for BOTDA measurement of deformations of geotechnical structures and error analysis. Measurement 146, 618–627.

Greening, Landscape and Tree Management Section, Development Bureau, 2013. Management Guidelines for Stonewall Trees. https://www.greening.gov.hk/filemanager/content/pdf/tree_care/Guilelines_for_stone_wall_trees_e.pdf.

Hassinen, A., Lemettinen, M., Peltola, H., Kellomäki, S., Gardiner, B., 1998. A prism-based system for monitoring the swaying of trees under wind loading. Agric. For. Meteorol. 90 (3), 187–194.

Hill, K.O., Fujii, F., Johnson, D.C., Kawasaki, B.S., 1978. Photosensitivity on optical fiber waveguides: Application to reflection filter fabrication. Appl. Phys. 32, 647–649.

Hill, K.O., Meltz, G., 1997. Fiber Bragg grating technology fundamentals and overview. J. Light. Technol. 15 (8), 1263–1276.

Hong, C.Y., Zhang, Y.F., Zhang, M.X., Leung, L.M.G., Liu, L.Q., 2016. Application of FBG sensors for geotechnical health monitoring, a review of sensor design, implementation methods and packaging techniques. Sens. Actuators. A 244, 184–197.

Hong, C.Y., Zhang, Y.F., Li, G.W., Zhang, M.X., Liu, Z.X., 2017. Recent progress of using Brillouin distributed fiber optic sensors for geotechnical health monitoring. Sens. Actuators. A 258, 131–145.

James, K.R., Haritos, N., Ades, P.K., 2006. Mechanical stability of trees under dynamic loads. Am. J. Bot. 93 (10), 1522–1530.

Jim, C.Y., Chen, W.Y., 2010. Habitat effect on vegetation ecology and occurrence on urban masonry walls. Urban For. Urban Green. 9 (3), 169–178.

Kane, B., Clouston, P., 2008. Tree pulling tests of large shade trees in the genus Acer. Arboric Urban For 34 (2), 101.

Katsuda, Y., Sugimoto, S., Ishizuka, Y., Iwasaki, S., Takaesu, R., Yamanaka, M., 2019. Development of the deformation monitoring system with wireless sensor network and evaluation of mechanical stability for damaged stonewalls. Int. J. Geomate. 17 (63), 1–8.

Li, H.J., Zhu, H.H., Li, Y.H., Hu, W., Shi, B., 2020. Fiber Bragg grating-based flume test to study the initiation of landslide-debris flows induced by concentrated runoff. Geotech. Test. J. 44 (4). https://doi.org/10.1520/GTJ20190290.

Liu, C., Zhang, S.Y., Cloutier, A., Rycabel, T., 2007. Modeling lumber bending stiffness and strength in natural black spruce stands using stand and tree characteristics. For. Ecol. Manag. 242 (2–3), 648–655.

Morey, W.W., Meltz, G., Glenn, W.H., 1990. Fiber optic Bragg grating sensors. In: Fiber Optic and Laser Sensors VII. International Society for Optics and Photonics, pp. 98–107.

Ni, P., Moore, I.D., Take, W.A., 2018. Distributed fibre optic sensing of strains on buried full-scale PVC pipelines crossing a normal fault. Géotechnique 68 (1), 1–17.

Park, H.S., Lee, H.M., Adeli, H., Lee, I., 2007. A new approach for health monitoring of structures: terrestrial laser scanning. Comput.-Aided Civil Infrastruct. Eng. 22 (1), 19–30.

Pei, H.F., Teng, J., Yin, J.H., Chen, R., 2014. A review of previous studies on the applications of optical fiber sensors in geotechnical health monitoring. Measurement 58, 207–214.

Pei, H.F., Yin, J.H., Jin, W., 2013. Development of novel optical fiber sensors for measuring tilts and displacements of geotechnical structures. Meas. Sci. Technol. 24 (9), 095202.

Peltola, H., Kellomaki, S., Vaisanen, H., Ikonen, V.P., 1999. A mechanistic model for assessing the risk of wind and snow damage to single trees and stands of Scots pine, Norway spruce, and birch. Can. J. For. Res. 29, 647–661.

Powrie, W., Harkness, R.M., Zhang, X., Bush, D.I., 2002. Deformation and failure modes of drystone retaining walls. Géotechnique 52 (6), 435–446.

Qin, J.Q., Feng, W.Q., Wu, P.C., Yin, J.H., 2020. Fabrication and performance evaluation of a novel FBG-based effective stress cell for directly measuring effective stress in saturated soils. Measurement 155, 107491.

Shi, X.S., Liu, K., Yin, J., 2021. Effect of initial density, particle shape, and confining stress on the critical state behavior of weathered gap-graded granular soils. J. Geotech. Geoenviron. Eng. 147 (2), 04020160.

Staszewski, W.J., Lee, B.C., Mallet, L., Scarpa, F., 2004. Structural health monitoring using scanning laser vibrometry: I. Lamb wave sensing. Smart Mater. Struct. 13 (2), 251.

Wu, P.C., Tan, D.Y., Chen, W.B., Malik, N., Yin, J.H., 2021. Novel fiber Bragg Grating-based strain gauges for monitoring dynamic responses of Celtis sinensis under typhoon conditions. Measurement 172, 108966.

Xiong, H., Yin, Z.Y., Nicot, F., Wautier, A., Marie, M., Darve, F., Guillaume, V., Philippe, P., 2021. A novel multi-scale large deformation approach for modelling of granular collapse. Acta Geotech 16, 2371–2388.

Xu, D.S., Liu, H.B., Luo, W.L., 2018. Development of a novel settlement monitoring system using fiber-optic liquid-level transducers with automatic temperature compensation. IEEE Trans. Instrum. Meas. 67 (9), 2214–2222.

Xu, D.S., Yin, J.H., Cao, Z.Z., Wang, Y.L., Zhu, H.H., Pei, H.F., 2013. A new flexible FBG sensing beam for measuring dynamic lateral displacements of soil in a shaking table test. Measurement 46 (1), 200–209.

Zhang, C.C., Zhu, H.H., Liu, S.P., Shi, B., Zhang, D., 2018. A kinematic method for calculating shear displacements of landslides using distributed fiber optic strain measurements. Eng. Geol. 234, 83–96.

Zhang, C.C., Zhu, H.H., Liu, S.P., Shi, B., Cheng, G., 2020. Quantifying progressive failure of micro-anchored fiber optic cable–sand interface via high-resolution distributed strain sensing. Can. Geotech. J. 57 (6), 871–881.

Zhang, L., Shi, B., Zhu, H.H., Yu, X.B., Han, H., Fan, X., 2021. PSO-SVM-based deep displacement prediction of Majiagou landslide considering the deformation hysteresis effect. Landslides 18 (1), 179–193.

Zhang, P., Chen, R.P., Wu, H.N., 2019. Real-time analysis and regulation of EPB shield steering using random forest. Autom. Constr. 106, 101860.

Zhu, H.H., Shi, B., Zhang, J., Yan, J.F., Zhang, C.C., 2014. Distributed fiber optic monitoring and stability analysis of a model slope under surcharge loading. J. Mt. Sci. 11 (4), 979–989.

Zhu, H.H., Shi, B., Zhang, C.C., 2017a. FBG-based monitoring of geohazards: current status and trends. Sensors 17 (3), 452.

Zhu, H.H., Zhang, C.C., Mei, G.X., Shi, B., Gao, L., 2017b. Prediction of one-dimensional compression behavior of Nansha clay using fractional derivatives. Mar. Georesources Geotechnol. 35 (5), 688–697.

Daoyuan Tan obtained his BEng and MPhil degrees from the China University of Geosciences, China, in 2011 and 2014, respectively, and PhD in Geotechnical Engineering from The Hong Kong Polytechnic University, Hong Kong, China, in 2019. He was affiliated as a post-doc fellow from 2019 to 2020 and is currently a Research Assistant Professor in the Department of Civil and Environmental Engineering of the Hong Kong Polytechnic University since 2020. His research interests include geohazard management, development and application of optic fibre sensing technology in geotechnical engineering practice, and intelligent monitoring of geotechnical structures.